A Semi-Empirical Tire-Model Including the Effects of Camber

Svendenius, Jacob; Gäfvert, Magnus

2004

Document Version:
Publisher's PDF, also known as Version of record

ISSN 0280–5316
ISRN LUTFD2/TFRT--7611--SE

A Semi-Empirical Tire-Model Including the Effects of Camber

Jacob Svendenius
Magnus Gäfvert

Department of Automatic Control
Lund Institute of Technology
December 2004

Department of Automatic Control
Lund Institute of Technology
Box 118
SE-221 00 Lund Sweden

Document name
INTERNAL REPORT

Date of issue
December 2004

Document Number
ISRN LUTFD2/TFRT--7611--SE

Author(s)
Jacob Svendenius
Magnus Gäfvert

Supervisor
Björn Wittenmark

Sponsoring organisation
Haldex Brake Products AB

Title and subtitle
A Semi-Empirical Tire-Model Including the Effects of Camber

Abstract

This report presents the addition of camber to a previously published semi-empirical tire model by the same authors. The model combines empirical models for pure braking, cornering and cambering to a model for simultaneous braking, cornering and cambering. It is based on brush-model tire mechanics and aims to offer an easy-to-use accurate model for vehicle handling-simulations. The proposed model is a method to extract and rescale the adhesion and sliding forces from empirical pure-slip tire models to account for the combined-slip condition. The combined-slip self-aligning torque is described likewise. Cambering affects the natural path of the tire carcass on the road surface and deforms the threads to produce an additional force in the lateral direction. Thereby, the proportions of the sliding and adhesive forces changes. The model is computationally sound and efficient and does not rely on any additional parameters that depend on combined-slip data for calibration. It can be used in combination with virtually any empirical pure-slip model. The report also contains a validation of the combined slip behavior towards measurement data from a Jeep Cherokee equipped with Goodyear-wrangler tires.

Key words
Tire model; Camber; Combined slip; Tire forces; Brush model

Classification system and/or index terms (if any)

Supplementary bibliographical information

ISSN and key title
0280–5316

ISBN

Language
English

Number of pages
24

Recipient's notes

Security classification

Contents

1. Introduction

The forces generated in the contact between the tires and the road are of major importance for the dynamic behavior of a road vehicle. Hence, accurate tire models are necessary components of complete vehicle models aimed at analyzing or simulating vehicle motion in real driving conditions. This article describes an extension to the semi-empirical tire model presented in [2], which combines empirical models for pure braking and cornering to derive the tire forces for simultaneous braking and cornering.

The method is based on the theory from the brush model with assumption on parabolic pressure distribution, which is a standard approach to describe tire behavior [1, 5, 9]. The brush model describes the generation of tire forces by dividing the contact patch into regions of adhesion and sliding. The rubber volume between the tire and the road surface is partitioned into infinitesimal elements in the form of elastic bristles. Each bristle is assumed to deform independently and linearly elastic in the longitudinal and lateral directions. In the adhesion region the bristles adhere to the road surface. Thus, the deformation force is carried by static friction. When a bristle comes in contact with the road it is undeformed. Due to the velocity difference between the road and the carcass the bristle deforms during its travel through the contact patch. At a certain point, called the break-away point x_s, the deformation force exceeds the friction force and the bristle starts to slide and carries a kinetic friction force.

Analytical expressions can be established for the force contributions, in each direction, from the adhesive and sliding regions, depending on the tire slip defined as

$$\sigma_x = \frac{v_x - \Omega R_e}{\Omega R_e}; \quad \sigma_y = \frac{v_y}{\Omega R_e}; \quad \bar{\sigma} = (\sigma_x, \sigma_y) \tag{1}$$

where v_x is the longitudinal motion of the wheel rim and v_y is the lateral motion of the wheel rim. The dynamic radius of the tire is denoted by R_e and Ω is the rotation velocity of the rim. At very low slips the resulting tire force is proportional to the slip. The coefficient of proportion is in the longitudinal direction called braking stiffness, C_x, and in the lateral direction, cornering stiffness, C_y. These depend on the contact patch length, $2a$, and the tire tread stiffness, c_{px} and c_{py}, as

$$C_x = 2c_{px}a^2; \qquad C_y = 2c_{py}a^2 \tag{2}$$

2. The Effect of Cambering on the Brush-Model

Camber denotes tilting of the tire in the x-direction, see Figure 1. The effects from cambering are particularly important when deriving models for motorcycles that produces a large part of the cornering force by tilting. For cars and, in particular, trucks the cambering angles are much smaller and in many applications their effect can be neglected. However, some suspension designs make the wheels to camber when the axle load varies. Elasticity in beams, bolts and axles can also allow cambering during cornering. Cambering of a tire creates a lateral force, even though there is no lateral slip. The developed tire force due to tilting of the tire, can with some

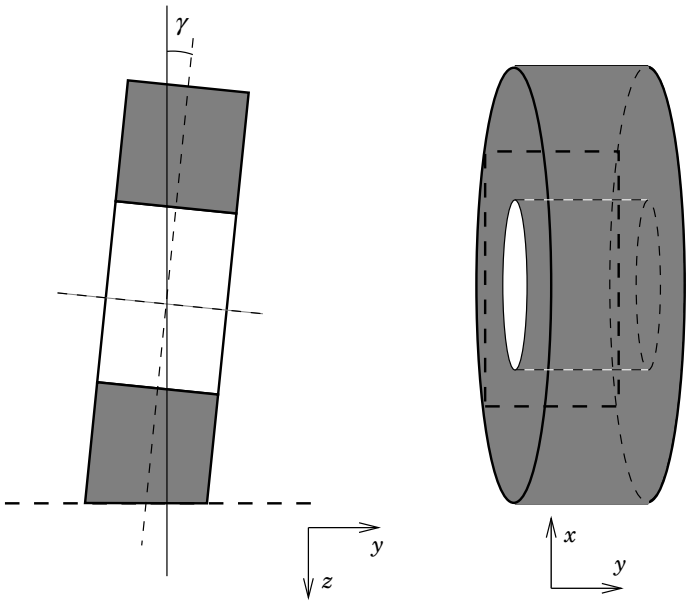

Figure 1 Cambered wheel. Left: Rear view; Right: Top view with contact patch (dashed rectangle). Note that the contact patch is greatly exaggerated in size.

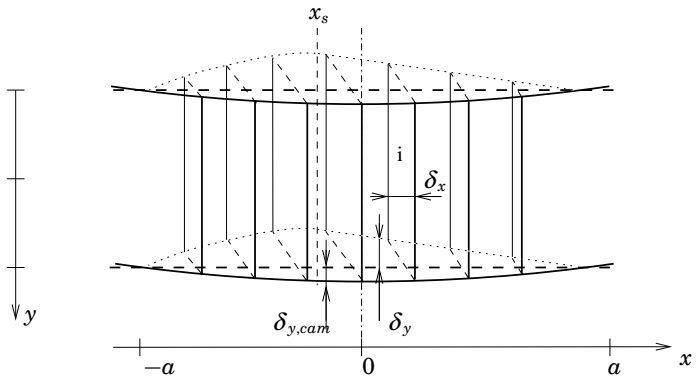

Figure 2 Schematic illustration of the contact patch showing the bristle deformation due to longitudinal and lateral slip and cambering.

approximations, be explained by the brush model. In Figure 1 a cambered tire is shown together with the orbit, an ellipse, that describes the projection on the road surface of a point on the carcass during rolling motion. The most common sign convention of γ is that positive angles are tilting out from the vehicle. Here, clockwise rotation around the x-axis is positive. The deviation from the straight contact patch from a non-cambered tire is

$$y = -\sin(\gamma)\left(\sqrt{R^2 - x^2} - \sqrt{R^2 - a^2}\right) \tag{3}$$

where R is the average wheel radius and a is half the contact length. Figure 2 also shows the deformation of bristle element due to cambering and lateral slip according to the brush model. Relation (3) will result in difficult expressions when the standard parabolic pressure distribution is employed for the brush-model. In, for example, [1] and [6] the deviation

due to cambering is approximated as a parabolic function similar to the assumed pressure distribution as

$$\delta_{y,cam}(x) = -\gamma k \left(a^2 - x^2\right) \tag{4}$$

where k is chosen such that the average camber deflection is correct in the contact patch

$$\int_{-a}^{a} \delta_{y,cam} dx = \int_{-a}^{a} y dx \Rightarrow k \approx \frac{3}{4} \frac{R - \sqrt{R^2 - a^2}}{a^2} \tag{5}$$

The approximation simplifies the calculations considerably. The deformation of a bristle that adheres to the road in the contact patch is then $-\delta_{y,cam}$ and the total bristle deformation including the effects caused by slip can be written as

$$\delta_x(x) = -\sigma_x(a - x); \quad \delta_y(x) = -\sigma_y(a - x) + \gamma k(a^2 - x^2) \tag{6}$$

2.1 Size of the adhesive region

A fundamental idea of the brush model is the partitioning of the contact patch into one adhesive and one sliding region. The size of the adhesive region is determined by the amount of available static friction. A bristle will start to slide when the force required for the deformation is larger than the available friction force. The following condition has to be fulfilled for adhesion

$$\left(\frac{dF_{ax}(x)}{dF_z(x)\mu_{\mathrm{sx}}}\right)^2 + \left(\frac{dF_{ay}(x)}{dF_z(x)\mu_{\mathrm{sy}}}\right)^2 \leq 1 \tag{7}$$

where the static friction coefficient in each direction is μ_{sx} and μ_{sy} and the normal force acting on a bristle is dF_z. The adhesive bristle forces are derived from the deflection as

$$dF_{ax} = c_{px}\delta_x(x)dx; \qquad dF_{ay} = c_{py}\delta_y(x)dx \tag{8}$$

where c_{px} and c_{py} are the rubber stiffnesses in respective direction. Using (4), (7) and (8) an expression for computation of the break-away point can be derived as

$$\sqrt{\left(\frac{c_{px}\sigma_x}{\mu_{sx}}\right)^2 + \left(\frac{c_{py}\left(\sigma_y + \gamma k(a + x_s)\right)}{\mu_{sy}}\right)^2}(a - x_s) \leq q_z(x_s) \tag{9}$$

Assume the parabolic pressure distribution

$$q_z(x) = \frac{3F_z}{4a}\left(1 - \left(\frac{x}{a}\right)^2\right) \tag{10}$$

and define the normalized slip, ψ, as

$$\psi(\sigma_x, \sigma_y, \gamma) \triangleq \frac{\gamma^{\circ 2}}{\gamma^{\circ 2} - \gamma^2}\left(\frac{\sigma_y\gamma}{\sigma_y^\circ\gamma^\circ} + \sqrt{\left(\frac{\sigma_x}{\sigma_x^\circ}\right)^2 + \left(\frac{\sigma_y}{\sigma_y^\circ}\right)^2 - \left(\frac{\sigma_x\gamma}{\sigma_x^\circ\gamma^\circ}\right)^2}\right) \tag{11}$$

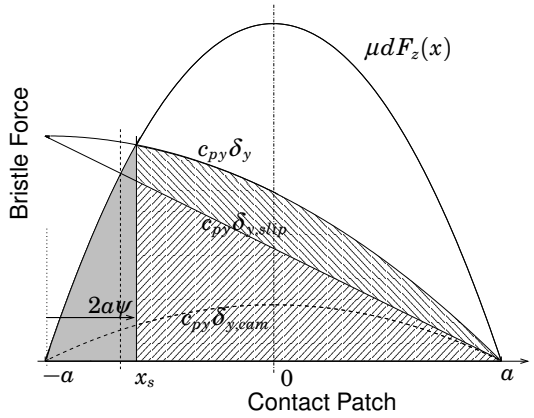

Figure 3 Force generation in the contact patch due to slip and camber. The shaded area is the force generated in the sliding region. The lower area with diagonal lines denotes the adhesion force generated by slip and the upper the contribution due to camber. The dashed straight line indicates the sliding region in case of zero camber.

where the limit slips, σ_x°, σ_x°, and the camber limit angle γ° are defined as

$$\sigma_x^\circ \triangleq \frac{3F_z\mu_{sx}}{2a^2c_{px}}; \qquad \sigma_y^\circ \triangleq \frac{3F_z\mu_{sy}}{2a^2c_{py}}; \qquad \gamma^\circ \triangleq \frac{3F_z\mu_{sy}}{2C_yka} \tag{12}$$

Then the break-away point can be written as

$$x_s(\sigma_x, \sigma_y, \gamma) = (2\psi(\sigma_x, \sigma_y, \gamma) - 1)\, a \tag{13}$$

The partitioning of the contact patch and the significance of ψ and x_s is visualized in Figure 3. It is clear that values of ψ larger than unity lack physical interpretation. Since the bristle deformation due to cambering has the same shape as the pressure distribution along the contact patch, ψ will be zero as long as $\sigma_x = \sigma_y = 0$. At the camber angle γ° the whole contact patch starts to slide against the road and ψ can not be computed since the denominator reaches zero. In this case the model is not valid and if accurate results are to be obtained a different tire model should be used. It is pointed out that such large camber angles are not relevant for studies on trucks and cars.

2.2 Forces

The forces generated in the contact patch are derived separately for the adhesive and sliding regions. For small slips the force is mainly generated by deformation of the rubber threads and for higher slip the major part is from sliding. When $\psi \geq 1$ the entire surface is sliding and there is no adhesive-force contribution.

Adhesion The forces generated in the adhesive region is the sum of the force contribution from each bristle. The tire forces developed by the slip are

$$F_{ax}(\sigma_x, \sigma_y, \gamma) = -C_x\sigma_x \left(1 - \psi(\sigma_x, \sigma_y, \gamma)\right)^2 \tag{14a}$$

$$F_{ay,slip}(\sigma_x, \sigma_y, \gamma) = -C_y \sigma_y \left(1 - \psi(\sigma_x, \sigma_y, \gamma)\right)^2 \tag{14b}$$

where $C_x = 2c_{px}a^2$ and $C_y = 2c_{py}a^2$ are the braking and cornering stiffnesses. The force generated by camber can be computed as

$$\begin{aligned} F_{\text{cam}}(\sigma_x, \sigma_y, \gamma) &= \int_{x_s(\sigma_x,\sigma_y,\gamma)}^{a} c_{py}\gamma k(a^2 - x^2)dx \\ &= \frac{2}{3}\gamma k a C_y \left(2\psi^3(\sigma_x, \sigma_y, \gamma) - 3\psi^2(\sigma_x, \sigma_y, \gamma) + 1\right) \end{aligned} \tag{15}$$

The camber stiffness, C_γ is defined as

$$C_\gamma = \left.\frac{\partial F_y(0, 0, \gamma)}{\partial \gamma}\right|_{\gamma=0} = \frac{2kaC_y}{3} = \frac{F_z \mu_{sy}}{\gamma^\circ} \tag{16}$$

In case of pure cambering for $\gamma < \gamma^\circ$ the lateral force is

$$F_{0\text{cam}}(\gamma) = C_\gamma \gamma \tag{17}$$

The total adhesive lateral force is

$$F_{ay}(\sigma_x, \sigma_y, \gamma) = F_{ay,slip}(\sigma_x, \sigma_y, \gamma) + F_{\text{cam}}(\sigma_x, \sigma_y, \gamma) \tag{18}$$

Sliding The normal force acting on the sliding region at partial sliding may be computed from (10) and (13) as

$$F_{sz}(\sigma_x, \sigma_y, \gamma) = \int_{-a}^{x_s(\sigma_x,\sigma_y,\gamma)} q_z(x)\, dx = F_z \psi^2(\sigma_x, \sigma_y, \gamma)\left(3 - 2\psi(\sigma_x, \sigma_y, \gamma)\right) \tag{19}$$

In the sliding region the forces are described by sliding friction characteristics. In the general case of anisotropic sliding friction, different methods can be applied to derive the angle and magnitude of the resulting force. This is further explained in [2]. Here, a method that makes the sliding-friction force collinear with the slip velocity is used. The forces generated in the sliding region are given by

$$F_{sx}(\sigma_x, \sigma_y, \gamma) = -\cos(\beta')\mu_{kx} F_{sz}(\sigma_x, \sigma_y, \gamma) \tag{20a}$$

$$F_{sy}(\sigma_x, \sigma_y, \gamma) = -\sin(\beta')\mu_{ky} F_{sz}(\sigma_x, \sigma_y, \gamma) \tag{20b}$$

where

$$\tan(\beta') = \frac{\mu_{kx}\sigma_y}{\mu_{ky}\sigma_x} \tag{21}$$

During the travel of a bristle through the sliding area the deformation, δ_x, δ_y, changes, since the vertical force on the bristle varies according to the parabolic pressure distribution. The rate of change of the deformation is small and the effect on the sliding velocity is neglected. The curvature of the bristle path resulting from cambering is small for small camber angles and the effect on the sliding friction forces is neglected. In other words, the only effect cambering has on the sliding force is that it changes the size of the sliding region.

2.3 Self-aligning torque

The self-aligning torque is the torque developed by non-symmetric bristle deformation in the contact patch. For pure slip the torque can be calculated in one part from the adhesion area and one part from the sliding region as

$$M_{az}(\sigma_x, \sigma_y, \gamma) = -c_{py} a^3 \sigma_y \frac{2}{3} \left(1 - \psi(\sigma_x, \sigma_y, \gamma)\right)^2 \left(4\psi(\sigma_x, \sigma_y, \gamma) - 1\right) \quad (22)$$

$$M_{sz}(\sigma_x, \sigma_y, \gamma) = -3\mu_{kx} \sin(\beta) a F_z \psi^2(\sigma_x, \sigma_y, \gamma) \left(1 - \psi(\sigma_x, \sigma_y, \gamma)\right)^2 \quad (23)$$

which is further explained in [2]. At combined slip a second order effect, due to the tire-carcass deformation, affects the torque as

$$M_{z,add}(\sigma_x, \sigma_y, \gamma) = F_x(\sigma_x, \sigma_y, \gamma) F_y(\sigma_x, \sigma_y, \gamma) \left(\frac{1}{C_{cx}} - \frac{1}{C_{cy}}\right) \quad (24)$$

where C_{cx} and C_{cy} are the carcass stiffness coefficients. The effect is described more detailed in [8].

According to the conditions assumed in this report pure cambering will not give rise to any self-aligning torque. As long as there is no sliding region in the contact patch the bristle deformation is symmetric. A simultaneous slip causes a sliding region and the contribution to the torque due to camber in the adhesive region can be written as

$$M_{z,cam} = \int_{x_s(\sigma_x,\sigma_y,\gamma)}^{a} c_{py} x \delta_{y,cam} dx = 2\gamma k a^2 C_y \psi^2(\sigma_x, \sigma_y, \gamma) \left(1 - \psi(\sigma_x, \sigma_y, \gamma)\right)^2 \quad (25)$$

3. The Combined-Slip Semi-Empirical Model

The general idea of the method to derive the forces at a combined slip $(\sigma_x, \sigma_y, \gamma)$ is to scale the forces from the empirical pure-slip model at certain pure slips $\sigma_{0x}(\sigma_x, \sigma_y, \gamma)$ and $\sigma_{0y}(\sigma_x, \sigma_y, \gamma)$. The pure slips can be chosen in various ways, but their relation to σ_x, σ_y and γ has to be well motivated and different proposals are discussed below. For convenience the arguments $(\sigma_x, \sigma_y, \gamma)$ for σ_{0x} and σ_{0y} are left out in the following. The scale factors depend on the combined longitudinal and lateral slip, the camber angle, and the relation between the used pure slip and the cambered combined slip, also for the scale factors the arguments $(\sigma_x, \sigma_y, \gamma)$ will be left out. Since the generation of forces from the adhesive and the sliding regions are built on different physical phenomena they are treated separately. The following equation shows the form

$$\hat{F}_x(\sigma_x, \sigma_y, \gamma) = G_{ax} \hat{F}_{0x}(\sigma_{0xa}) + G_{sx} \hat{F}_{0x}(\sigma_{0xs}) \quad (26)$$

$$\hat{F}_y(\sigma_x, \sigma_y, \gamma) = G_{ay} \hat{F}_{0y}(\sigma_{0ya}) + G_{sy} \hat{F}_{0y}(\sigma_{0ys}) + G_{\mathrm{cam}y} \hat{F}_{0\mathrm{cam}}(\gamma) \quad (27)$$

where $\hat{F}_{0j}$ are the empirical pure slip models and $\hat{F}_{0\mathrm{cam}}$ is the empirical pure cambering model, which may be as simple as the cambering stiffness, $\hat{C}_\gamma$, in combination with (17). If no information about the camber properties is available, then C_γ can be calculated from the cornering stiffness using (16). The half patch length a is either assumed or derived from (46)

using the aligning stiffness. The tire radius R and the contact patch length $2a$ is used to calculate k by Equation (5).

Analogously, the combined self-aligning torque can be derived as

$$M_z(\sigma_x, \sigma_y, \gamma) = G_{fz}\hat{F}_{0y}(\sigma_{0z}) + G_{mz}\hat{M}_{0z}(\sigma_{0z}) + G_{\mathrm{cam}z}\hat{F}_{0\mathrm{cam}}(\gamma) \tag{28}$$

The scale factors G_{ij} are derived from the analytical expressions of the brush model. For example

$$F_{ax}(\sigma_x, \sigma_y, \gamma) = \frac{F_{ax}(\sigma_x, \sigma_y, \gamma)}{F_{0x}(\sigma_{0xa})} F_{0x}(\sigma_{0xa}) = G_{ax}F_{0x}(\sigma_{0xa}) \approx G_{ax}\hat{F}_{0x}(\lambda_{0a}) \tag{29}$$

and

$$\begin{aligned} F_{ay}(\sigma_x, \sigma_y, \gamma) &= \frac{F_{ay}(\sigma_x, \sigma_y, \gamma)}{F_{0y}(\sigma_{0ya})} F_{0y}(\sigma_{0ya}) + \frac{F_{ay,cam}(\sigma_x, \sigma_y, \gamma)}{F_{0\mathrm{cam}}(\gamma)} F_{0\mathrm{cam}}(\gamma) \\ &= G_{ay}F_{0y}(\sigma_{0ya}) + G_{\mathrm{cam}y}F_{0\mathrm{cam}}(\gamma) \approx G_{ay}\hat{F}_{0y}(\sigma_{0ya}) + G_{\mathrm{cam}y}\hat{F}_{0\mathrm{cam}}(\gamma) \end{aligned} \tag{30}$$

3.1 Scale factors

Adhesive region The bristle deformations are the source of the adhesion forces. Therefore, for adhesion forces it makes sense to regard pure slips that result in the same deformation as the combined slip. The deformation state depends on the slip, $\bar{\sigma}$. The pure slip is therefore constructed to maintain $\bar{\sigma}$ constant. Hence

$$\sigma_{0x} = \sigma_x; \quad \sigma_{0y} = \sigma_y \tag{31}$$

The scale factors G_{ax} and G_{ay} can now be calculated as

$$G_{ax} = \frac{3\left(1 - \psi(\sigma_x, \sigma_y, \gamma)\right)^2}{\Upsilon(\sigma_x, 0, 0)}; \quad G_{ay} = \frac{3\left(1 - \psi(\sigma_x, \sigma_y, \gamma)\right)^2}{\Upsilon(0, \sigma_y, 0)} \tag{32}$$

with

$$\Upsilon(x, y, z) \triangleq \psi^2(x, y, z) - 3\psi(x, y, z) + 3 \tag{33}$$

The scale factor of the camber force is

$$G_{\mathrm{cam}y} = 2\psi^3(\sigma_x, \sigma_y, \gamma) - 3\psi^2(\sigma_x, \sigma_y, \gamma) + 1 \tag{34}$$

when $\psi < 1$, otherwise $G_{\mathrm{cam}y} = 0$. Refer to A for the details on the computations performed here and further on.

Sliding region In the literature, slip-velocity is mentioned as a significant factor that influences the friction coefficient for a specific tire on a certain road foundation [9]. Therefore, it is reasonable to define the pure slip used for the sliding forces so that the slip velocity is invariant. The respective pure slips $(\sigma_{0x}^{\mathrm{vel}}, 0, 0)$ and $(0, \sigma_{0y}^{\mathrm{vel}}, 0)$ at the wheel-travel velocity v_0, with

$$\sigma_{0x}^{\mathrm{vel}} = \frac{v\sqrt{\sigma_x^2 + \sigma_y^2}\,\mathrm{sgn}(\sigma_x)}{v_0\sqrt{(1+\sigma_x)^2 + \sigma_y^2} - v\sqrt{\sigma_x^2 + \sigma_y^2}\,\mathrm{sgn}\,(\sigma_x)} \tag{35a}$$

$$\sigma_{0y}^{\mathrm{vel}} = \frac{v\sqrt{\sigma_x^2+\sigma_y^2}\,\mathrm{sgn}(\sigma_y)}{\sqrt{v_0^2\left((1+\sigma_x)^2+\sigma_y^2\right)-v^2(\sigma_x^2+\sigma_y^2)}} \tag{35b}$$

result in the same slip velocity, v_s, as the combined slip $(\sigma_x, \sigma_y, \gamma)$ at the wheel-travel velocity v. Note that v is the actual wheel travel velocity and v_0 the velocity at which the pure slip model is valid. The scaling factors G_{sx} and G_{sy} are

$$G_{sx} = |\cos(\beta')| \cdot \Gamma_x; \qquad G_{sy} = |\sin(\beta')| \cdot \Gamma_y \tag{36}$$

with

$$\Gamma_x \triangleq \begin{cases} \left(v_0\sqrt{(1+\sigma_x)^2+\sigma_y^2} - v\sqrt{\sigma_x^2+\sigma_y^2}\,\mathrm{sgn}(\sigma_x)\right)\Lambda\sigma_x^\circ\,\mathrm{sgn}(\sigma_{0x}^{\mathrm{vel}}) \\ \cdot\dfrac{\psi(\sigma_x,\sigma_y,\gamma)(3-2\psi(\sigma_x,\sigma_y,\gamma))}{v\Upsilon(\sigma_{0x}^{\mathrm{vel}},0,0)} & \text{if } \psi(\sigma_{0x}^{\mathrm{vel}},0,0)<1 \\ \psi^2(\sigma_x,\sigma_y,\gamma)(3-2\psi(\sigma_x,\sigma_y,\gamma)) & \text{if } \psi(\sigma_{0x}^{\mathrm{vel}},0,0)\geq 1 \end{cases} \tag{37a}$$

and

$$\Gamma_y \triangleq \begin{cases} \left(v_0^2\left((1+\sigma_x)^2+\sigma_y^2\right)-v^2(\sigma_x^2+\sigma_y^2)\right)^{\frac{1}{2}}\Lambda\sigma_y^\circ\,\mathrm{sgn}(\sigma_{0y}^{\mathrm{vel}}) \\ \cdot\dfrac{\psi(\sigma_x,\sigma_y,\gamma)(3-2\psi(\sigma_x,\sigma_y,\gamma))}{v\Upsilon(0,\sigma_{0y}^{\mathrm{vel}},0)} & \text{if } \psi(0,\sigma_{0y}^{\mathrm{vel}},0)<1 \\ \psi^2(\sigma_x,\sigma_y,\gamma)(3-2\psi(\sigma_x,\sigma_y,\gamma)) & \text{if } \psi(0,\sigma_{0y}^{\mathrm{vel}},0)\geq 1 \end{cases} \tag{37b}$$

and

$$\Lambda \triangleq \frac{\gamma^{\circ 2}}{\gamma^{\circ 2}-\gamma^2}\left(\sin(\beta)\sigma_y^\circ\frac{\gamma}{\gamma^\circ}+\sqrt{\left(\frac{\cos(\beta)}{\sigma_x^\circ}\right)^2+\left(\frac{\sin(\beta)}{\sigma_y^\circ}\right)^2-\left(\frac{\cos(\beta)\gamma}{\sigma_x^\circ\gamma^\circ}\right)^2}\right) \tag{38}$$

if $\psi(\sigma_x, \sigma_y, \gamma) < 1$, otherwise

$$\Gamma_x \triangleq \begin{cases} \psi^{-1}(\sigma_{0x}^{\mathrm{vel}},0,0)\Upsilon^{-1}(\sigma_{0x}^{\mathrm{vel}},0,0) & \text{if } \psi(\sigma_{0x}^{\mathrm{vel}},0,0)<1 \\ 1 & \text{if } \psi(\sigma_{0x}^{\mathrm{vel}},0,0)\geq 1 \end{cases} \tag{39a}$$

and

$$\Gamma_y \triangleq \begin{cases} \psi^{-1}(0,\sigma_{0y}^{\mathrm{vel}},0)\Upsilon^{-1}(0,\sigma_{0y}^{\mathrm{vel}},0) & \text{if } \psi(0,\sigma_{0y}^{\mathrm{vel}},0)<1 \\ 1 & \text{if } \psi(0,\sigma_{0y}^{\mathrm{vel}},0)\geq 1 \end{cases} \tag{39b}$$

The friction-constraint angle β' can be derived from

$$\tan(\beta') = \frac{\sigma_y\Gamma_x\hat{F}_{0x}(\sigma_{0x}^{\mathrm{vel}})}{\sigma_x\Gamma_y\hat{F}_{0y}(\sigma_{0y}^{\mathrm{vel}})} \tag{40}$$

Self-aligning torque For simplicity, another pure-slip definition is used for the self-aligning torque. The pure slips $(\sigma_{0x}^{\mathrm{reg}}, 0, 0)$ and $(0, \sigma_{0y}^{\mathrm{reg}}, 0)$, with

$$\sigma_{0x}^{\mathrm{reg}} = \sigma_x^{\circ}\psi(\sigma_x, \sigma_y, \gamma)\,\mathrm{sgn}(\sigma_x)\,; \qquad \sigma_{0y}^{\mathrm{reg}} = \sigma_y^{\circ}\psi(\sigma_x, \sigma_y, \gamma)\,\mathrm{sgn}(\sigma_y) \tag{41}$$

result in adhesion and sliding regions of the same size as the combined slip $(\sigma_x, \sigma_y, \gamma)$. The self-aligning torque is derived as

$$M_z(\sigma_x, \sigma_y, \gamma) = G_{fz}F_{0y}(\sigma_y^{\mathrm{reg}}) + G_{mz}M_{0z}(\sigma_y^{\mathrm{reg}}) + G_{\mathrm{cam}z}F_{0\mathrm{cam}}(\gamma) \tag{42}$$

where

$$G_{mz} = \sin(\beta') \tag{43}$$

and

$$G_{fz} = \frac{a}{3}\frac{(4\psi - 1)(1 - \psi)^2}{\Upsilon}\left(\frac{\sin(\beta)}{\sigma_y^{\circ}\Lambda} - \sin(\beta')\right), \tag{44}$$

$$G_{\mathrm{cam}z} = 3a\psi^2(\sigma_x, \sigma_y, \gamma)\left(1 - \psi(\sigma_x, \sigma_y, \gamma)\right)^2 \tag{45}$$

Note that the brush model states that the contact patch length can be derived by the relation between the cornering stiffness and the self-aligning stiffness as

$$C_z = -\left.\frac{\partial M_z}{\partial \sigma_y}\right|_{\sigma_x, \sigma_y = 0} = c_{py}a^3\frac{2}{3} = C_y\frac{a}{3} \tag{46}$$

When using the region-invariant slips the friction angle is computed from

$$\tan(\beta') = \frac{\sigma_y}{\sigma_x}\frac{\hat{F}_{0x}(\sigma_x^{\mathrm{reg}})}{\hat{F}_{0y}(\sigma_y^{\mathrm{reg}})} \tag{47}$$

3.2 Parameters

Four parameters are needed in the model, which all have clear physical interpretations. The parameters σ_x° and σ_y°, describe the pure slips where transition from partial to full sliding occur. They are needed to compute the normalized slip, $\psi(\sigma_x, \sigma_y, \gamma)$. A common assumption is that these transitions occur when the tire forces obtain their maxima. Some road foundations, such as gravel and snow might not provide a clear maximum point. In any case, the parameters may simply be set to the slip values corresponding to the maxima of the tire forces, F_{0x}^* and F_{0y}^*. From the brush model it can be shown that

$$\sigma_x^{\circ} \approx \frac{3F_{0x}^*}{C_x}; \qquad \sigma_y^{\circ} \approx \frac{2F_{0y}^*}{C_x} + \frac{F_{0y}^*}{C_y} \tag{48}$$

where the first relation is a result of (12). The lateral limit has been corrected for the carcass deflection, this is further discussed in [2]. The parameter v_0 denotes the wheel-travel velocity at which the empirical pure-slip model is valid. The actual wheel-travel velocity v is assumed to be a model input. If v_0 is not known then $v/v_0 = 1$ may be used, which will neglect any velocity dependence. This is the common assumption in most other models.

The camber parameter, γ°, is outside the cambering range that is normally measured on truck and car tires. Therefore, it is not possible to read it directly from measurement data. Instead it can be used that (16) is well approximated by $\gamma^{\circ} \approx F_{0y}^*/C_\gamma$. The camber stiffness can either be given from the empirical camber model or be computed from tire parameters according to (16) using (5) and (46).

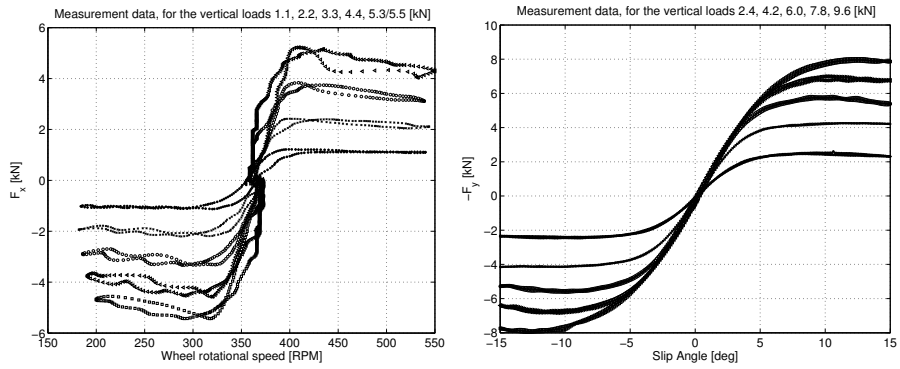

Figure 4 Available measurement data. Left: Longitudinal force for different wheel rotational speeds; Right: Lateral force for sweeps of α.

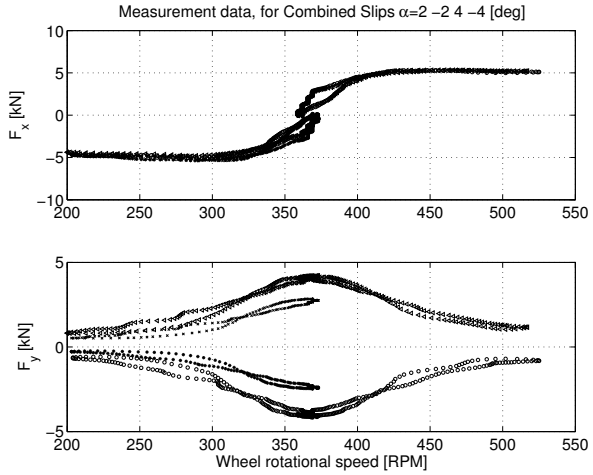

Figure 5 Available measurement data. Longitudinal and lateral force for combined slip at F_z=5.3/5.5 kN.

4. Results and Discussion

Empirical data, provided by NHTSA, US, for P225/75R15 Goodyear Wrangler RT/S, OWL, all terrain steel belted radials [7], are used for validation. The reference speed used was 45 km/h and inflation pressure 2.4 bar. The data consist of pure-slip forces and aligning moments in the slip ranges $\lambda = [-50, 50]\%$ and $\alpha = [-15, 15]$ deg. Forces at combined slip at $\alpha = [\pm 2, \pm 4]$ deg for sweeps of λ and forces at some camber angles were also included. The different vertical loads for the measurements of the pure longitudinal behavior are 1.1, 2.2, 3.3, 4.4, 5.5[1] kN, for the pure lateral and cambering behavior 2.4, 4.2, 6.0, 7.8, 9.6 kN. For the combined slip behaviour data was only collected at 5.5 kN (see footnote). The available measurement data are shown in Figures 4, 5 and 6.

[1]It is unclear from the data whether the highest load for sweeps of λ and also the combined slips is 5.3 kN or 5.5 kN

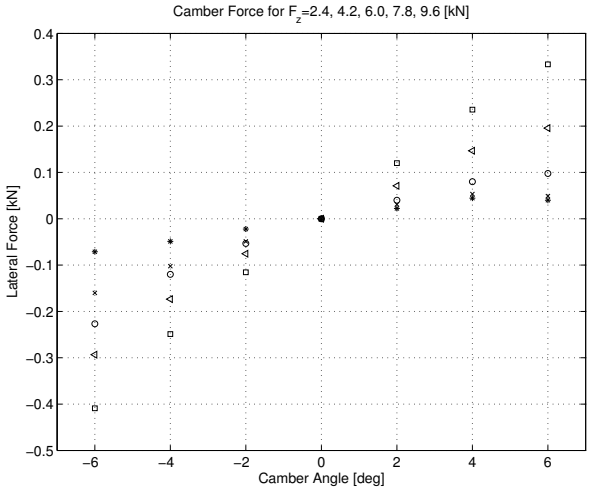

Figure 6 Lateral force as a function of the camber angle (γ) for different vertical loads.

4.1 Validation of the Semi-Empirical Model

The measurements of the pure lateral properties were performed at a different test bed than the longitudinal and combined properties. The vertical loads do not correspond between the test stands. The longitudinal pure slip model and the combined validation data are taken at highest available load and the lateral pure slip model at 6.0 kN. A linear correction is applied to adjust for the different loads. In Figure 7 the forces and torque from the model are compared to the measured values for sweeps of λ. The pure slip models are magic formula parameterizations of the raw data, but for the torque model interpolation of the tabular data was used. In Figure 8 only the pure slip measurement for sweep of α is showed together with the pure slip Magic Formula parameterization and the computed characteristics for combined slip. Figure 9 shows the force envelopes for sweeps of λ. The overall behavior of the model is very similar to the real measurements. Particularly good agreement is shown at small and large slips. The largest deviations can be found at slips around the force peak value. Since the tire behavior is sensitive to many factors it is very important that the pure slip empirical models are generated at the same conditions as the combined slip measurements. Change of measurement rigg and vertical load between the collection of data sets affects the reliability of the data and the validation.

4.2 Results of Cambering

The information about the camber properties for the tire was restricted to a few measurement points at different loads, see Figure 6. The parameters of interest for cambering are $C_y = 1.4$ kN/deg, $C_z = 54$ Nm/deg, and $C_\gamma = 26$ N/deg. It can be noticed that the influence of camber on the lateral tire force is very low for the tire, i.e. C_γ is small, and can be neglected for any practical case. Interestingly, the camber stiffness calculated from the cornering stiffness, as described in Section 3, is significantly larger, $C_\gamma = 120$ N/deg. To be able to visualize the effects of camber, the computed larger stiffness was chosen. In Figure 10 the effect of camber is shown

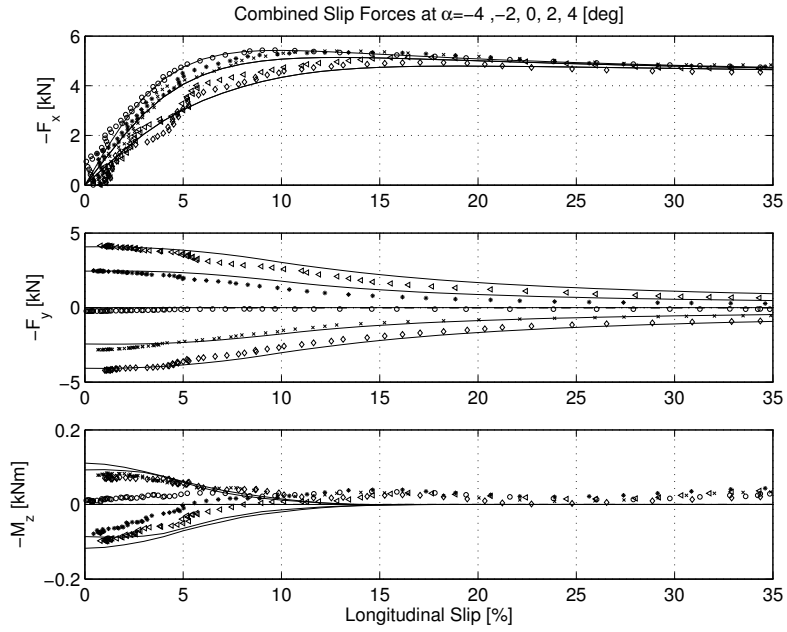

Figure 7 Combined measurement data compared to model for sweeps of λ at different slip angles.

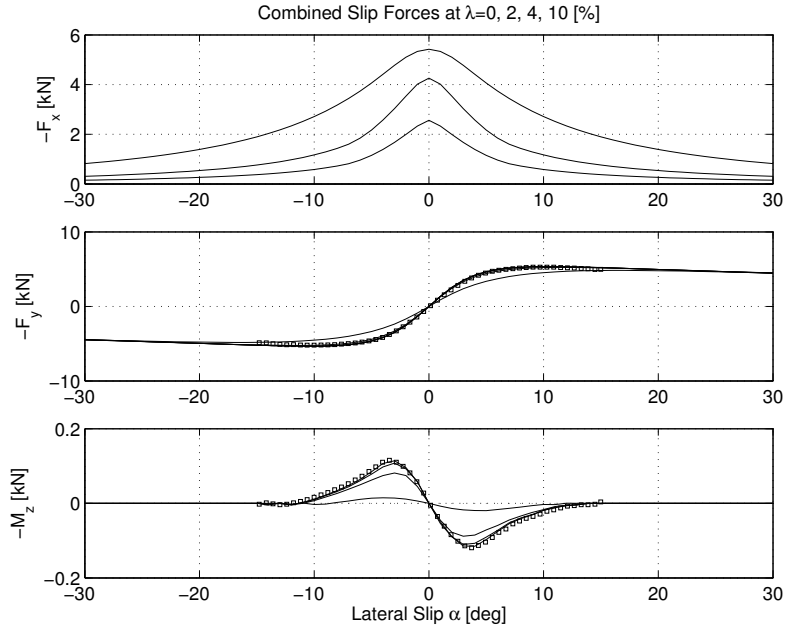

Figure 8 Lateral behavior for combined slip of the model. The measured data at pure slip is also showed.

for sweeps of λ and in Figure 11 for sweeps of α. It can be seen from the result that camber hardly affects the longitudinal force. It affects the partitioning between sliding and adhesion, but the lower adhesions force is compensated by a higher sliding force. In other tire models, for example presented in [3] the camber effect is included as a shift on the lateral slip, i.e. the lateral slip gets an additional term of $C_\gamma \gamma / C_y$. This much simpler

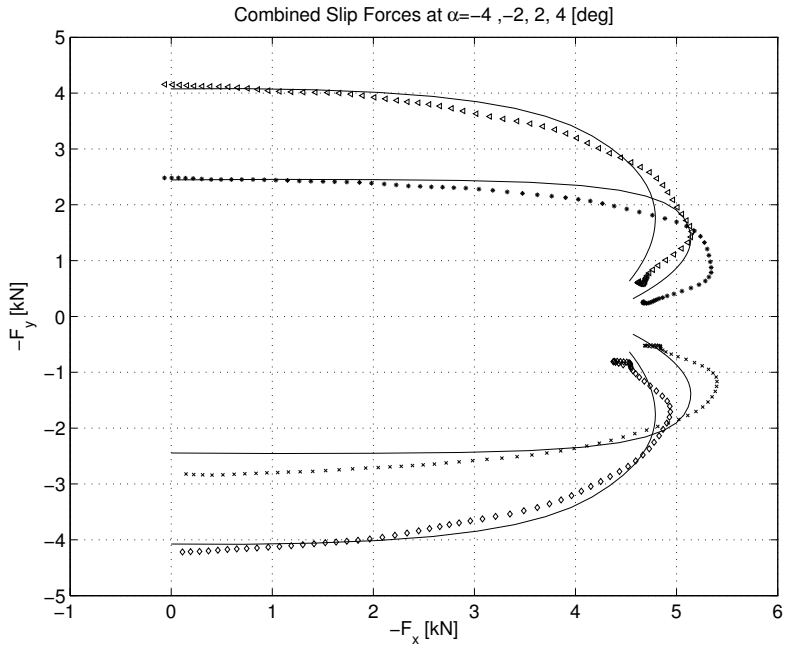

Figure 9 The longitudinal and lateral force at combined slip for sweeps of λ. Comparison of measured data and the proposed model (solid lines).

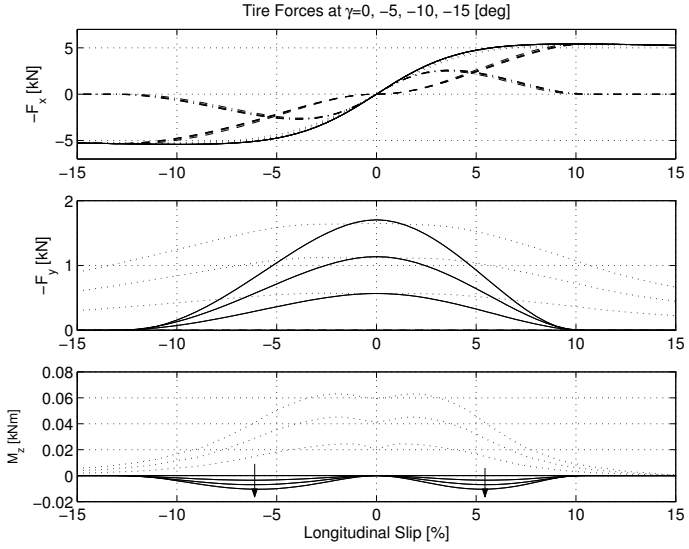

Figure 10 The effect of camber on the tire forces. The dashed dotted lines are the adhesion force and the dashed line the sliding forces. The camber effect when included as a shift on the lateral slip is shown by the dotted line for $\gamma = 0, -5, -10,$ and -15 deg.

approach to handle the camber is plotted in the figures and the results for pure slip cases are similar. For the combined-slip cases the results differ significantly because the offset has an undesired influence on the sliding velocity and hence on the sliding-force component. The self-aligning torque does also differ between the two methods. Figure 12 shows the camber effect on the lateral force as a function of the longitudinal tire force at

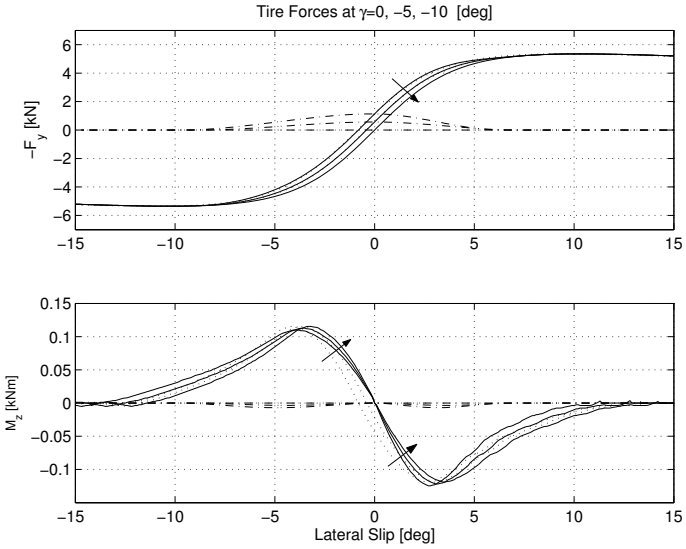

Figure 11 Illustration of the effects of camber on the tire forces. Solid lines are the total force and aligning torque. The dashed dotted lines are the camber forces. For the torque the dashed dotted lines denote the additional torque from the cambering forces. The camber effect when included as a shift on the lateral slip is shown by the dotted lines for $\gamma = 0, -5$, and -10 deg.

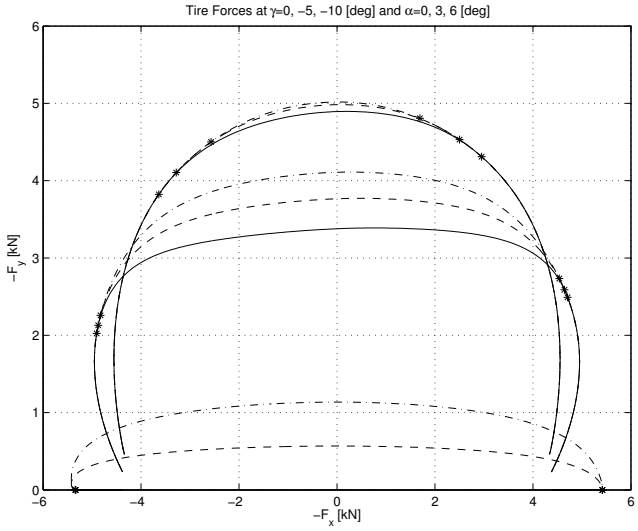

Figure 12 Illustration of the effects of camber on the lateral force as a function of the longitudinal tire force at combined slip. The solid lines shows zero camber, dashed lines $\gamma = -5$ deg and dashed-dotted lines $\gamma = -10$ deg. The transitions to full sliding are marked with asterisks.

combined slip. Note that camber has a strong influence on the point of transition to full sliding at larger lateral slip.

4.3 Discussion

The difference between the theoretical camber stiffness, $\hat{C}'_\gamma$ calculated from $2k\hat{C}_z$ where k is given by (5) using $a = 3\hat{C}_y/\hat{C}_z$ and the measured camber

Table 1 Comparison between measured and computed camber stiffness for different tires and loads. Note that $\hat{a}$ is calculated as $3\hat{C}_y/\hat{C}_z$ for all tires except 185/60 R14, where it is measured. The calculation is an approximation which gives unrealistic values at higher vertical loads.

	P225/75R15					*7.60-15* [5]			
F_z [kN]	2.4	4.2	6.0	7.8	9.6	2.5	4.5	6.3	8.1
R [m]			0.35				0.317		
$\hat{C}_y$ [kN/deg]	0.75	1.2	1.4	1.4	1.4	0.7	0.8	0.9	1
$\hat{C}_z$ [Nm/deg]	16	33	54	75	94	20	30	50	70
$\hat{a}$ [mm]	64	83	116	161	201	86	112	167	210
$\hat{C}_\gamma$ [N/deg]	9.2	17	26	40	61	100	125	133	145
$\hat{C}'_\gamma$ [N/deg]	40	82	135	187	235	50	75	125	175

	195/65 R15 [6]	*185/60 R14* [4]			*315/80 R22.5* [6]	*160/70ZR17* [6]
F_z	7	1.9	2.5	2.9	41	3
R	0.317		0.289		0.54	0.33
$\hat{C}_y$	1	1	1.2	1.4	4	0.5
$\hat{C}_z$	60	x	x	x	125	15
$\hat{a}$	180	75	87	96	94	90
$\hat{C}_\gamma$	100	30	45	50	$<$100	50
$\hat{C}'_\gamma$	150	62	87	112	312	37

stiffness, $\hat{C}_\gamma$ for six different tires is shown in Table 1. It is noticed that the deviation between the calculated and the measured camber stiffness is smaller for tires for personal cars and motorcycles than for tires for heavier vehicles as trucks or the Jeep, used in the example above. A theory that is discussed in [6] is that the assumed bristle deformation due to the camber is most accurate for tires with a rounded shoulder. For wider and flatter tires the camber effect might be better explained by deformation in the tire walls and changes in the contact pressure distribution instead of bristle deflections and carcass deformations. Such effects are, for example, discussed in [4] and are difficult to express using the brush model.

5. Conclusions

The generation of the camber force has been described in a simple manner, together with its influence on the partitioning of the sliding and adhesive regions in the tire contact patch. It has been shown that camber effects can be added to the previously published semi-empirical tire model by same authors, in a physically motivated way. For pure slips it is common to introduce camber by an offset on the lateral slip. However, for the self-aligning torque and the combined slip forces the proposed model gives significantly different result. It has also been discussed that the camber effects, with varying accuracy, can be approximated from the lateral properties of the tire.

6. Acknowledgements

This work was funded by Haldex Brake Products AB and the Swedish Research Council (contract 2001-3020). The authors are thankful to Prof. Björn Wittenmark for encouragement and support and to Kamel Saalani at the Transport Research center, Inc and Gary Heydinger at SEA, Inc for providing measurement data.

7. References

[1] G. Gim and P. E. Nikravesh. An analytical model of pneumatic tyres for vehicle dynamics simulations. part 2: Comprehensive slips. *International Journal of Vehicle Design*, 12(1):19–39, 1991.

[2] M. Gäfvert and J. Svendenius. A novel semi-empirical tire model for combined slip. Journal paper, to be published in Vehicle system dynamics, 2004.

[3] W. Hirschberg, G. Rill, and H. Weinfurter. User-appropriate tyre-modelling for vehicle dynamics in standard and limit situations. *Vehicle System Dynamics*, 38(2):103–125, 2002.

[4] Ichiro Kageyama and Satoru Kuwahara. A study on tire modeling for camber thrust and camber torque. JSAE Reveiw 23 pp. 325-331, 2002.

[5] H. B. Pacejka. Modelling of the pneumatic tyre and its impact on vehicle dynamic behavior. Technical Report i72B, Technische Universiteit Delft, 1988.

[6] H. B. Pacejka. *Tyre and Vehicle Dynamics*. Butterworth-Heinemann, 2002.

[7] K. Salaani, D Guenther, and G Heydinger. Vehicle dynamics modeling for the national advanced driving simulator of a 1997 jeep cherokee. SAE Paper No. 1999-01-0121, 1999.

[8] Jacob Svendenius and Magnus Gäfvert. A semi-empirical tire-model for transient combined-slip forces. In *AVEC '04*, August 2004.

[9] J. Y. Wong. *Theory of Ground Vehicles*. John Wiley & Sons, 3 edition, 2001.

A. Appendix

The derivation of the scale factors is only performed in the lateral direction, but the procedure for the longitudinal scale factors is similar.

A.1 Adhesive slip scale factors

$$
\begin{aligned}
G_{ay}(\sigma_x, \sigma_y, \gamma) &= \frac{F_{ay,slip}(\sigma_x, \sigma_y, \gamma)}{F_{0y}(\sigma_{0ya})} \\
&= \frac{-C_y \sigma_y (1 - \psi(\sigma_x, \sigma_y, \gamma))^2}{-C_y \sigma_y (1 - \psi(0, \sigma_y, 0))^2 - F_z \mu_y \sin(\beta) \psi^2(0, \sigma_y, 0) \, (3 - 2\psi(0, \sigma_y, 0))}
\end{aligned}
$$

$$= \frac{-C_y\sigma_y(1-\psi(\sigma_x,\sigma_y,\gamma))^2}{-C_y\sigma_y(1-\psi(0,\sigma_y,0))^2 - F_z\mu_y\sigma_y^\circ\frac{\sigma_y}{\sigma_y^\circ}\psi(0,\sigma_y,0)\,(3-2\psi(0,\sigma_y,0))}$$

$$= \frac{3\,(1-\psi(\sigma_x,\sigma_y,\gamma))^2}{\Upsilon(0,\sigma_y,0)} \quad (49)$$

when $\psi < 1$, otherwise $G_{ay}(\sigma_x,\sigma_y,\gamma) = 0$.

$$\Upsilon(x,y,z) \triangleq \psi^2(x,y,z) - 3\psi(x,y,z) + 3 \quad (50)$$

A.2 Camber scale factor

$$G_{camy}(\sigma_x,\sigma_y,\gamma)) = \frac{F_{camy}(\sigma_x,\sigma_y,\gamma)}{F_{0cam}(\gamma)} = 2\psi^3(\sigma_x,\sigma_y,\gamma) - 3\psi^2(\sigma_x,\sigma_y,\gamma) + 1 \quad (51)$$

A.3 Sliding scale factors

$$G_{sy}(\sigma_x,\sigma_y,\gamma) = \frac{F_{sy}(\sigma_x,\sigma_y,\gamma)}{F_{0y}(\sigma_{0ys})}$$

$$= \frac{-F_z\mu_y\sin(\beta')\psi^2(\sigma_x,\sigma_y,\gamma)\,(3-2\psi(\sigma_x,\sigma_y,\gamma))}{-C_y\sigma_{0y}^{\text{vel}}(1-\psi(0,\sigma_{0y}^{\text{vel}},0))^2 - F_z\mu_y\psi^2(0,\sigma_{0y}^{\text{vel}},0)\left(3-2\psi(0,\sigma_{0y}^{\text{vel}},0)\right)}$$

$$= \sin(\beta')\frac{\sigma_y^\circ}{\sqrt{\sigma_x^2+\sigma_y^2}\,\text{sgn}(\sigma_{0y}^{\text{vel}})}\frac{\psi^2(\sigma_x,\sigma_y,\gamma)(3-2\psi(\sigma_x,\sigma_y,\gamma))}{\Upsilon(0,\sigma_{0y}^{\text{vel}},0)}$$

$$\cdot\sqrt{\left(\frac{v_0}{v}\right)^2\left((1+\sigma_x)^2+\sigma_y^2\right) - (\sigma_x^2+\sigma_y^2)} \quad (52)$$

remark that

$$\Lambda = \frac{\psi(\sigma_x,\sigma_y,\gamma)}{\sqrt{\sigma_x^2+\sigma_y^2}}$$

$$\frac{\gamma^{\circ 2}}{\gamma^{\circ 2}-\gamma^2}\left(\sin(\beta)\sigma_y^\circ\frac{\gamma}{\gamma^\circ} + \sqrt{\left(\frac{\cos(\beta)}{\sigma_x^\circ}\right)^2 + \left(\frac{\sin(\beta)}{\sigma_y^\circ}\right)^2 - \left(\frac{\cos(\beta)\gamma}{\sigma_x^\circ\gamma^\circ}\right)^2}\right) \quad (53)$$

using

$$\sin(\beta) = \frac{\sigma_y}{\sqrt{\sigma_x^2+\sigma_y^2}}; \qquad \cos(\beta) = \frac{\sigma_x}{\sqrt{\sigma_x^2+\sigma_y^2}} \quad (54)$$

A.4 Scale factors for the self aligning torque

$$M_z(\sigma_x,\sigma_y,\gamma) = (M_{0z}(\sigma_y^{\text{reg}}) - t_{0a}(0,\sigma_y^{\text{reg}},0)F_{ay,slip}(0,\sigma_y^{\text{reg}},0))\sin(\beta')$$
$$+ t_a(\sigma_x,\sigma_y,\gamma)F_{ay,slip}(\sigma_x,\sigma_y,\gamma) + M_{z,cam}(\sigma_x,\sigma_y,\gamma)$$
$$= G_z(\sigma_x,\sigma_y,\gamma)M_{0z}(\sigma_y^{\text{reg}}) + G_{fz}(\sigma_x,\sigma_y,\gamma)F_{0y}(\sigma_y^{\text{reg}}) + G_{camz}\hat{F}_{0cam}(\gamma) \quad (55)$$

where

$$G_{mz} = \sin(\beta') \quad (56)$$

and

$$G_{fz} = \frac{t_a(\sigma_x,\sigma_y,\gamma)F_{ay,slip}(\sigma_x,\sigma_y,\gamma)}{F_{0y}(0,\sigma_y^{\text{reg}},0)} - \frac{t_{0a}(0,\sigma_y^{\text{reg}},0)F_{ay,slip}(0,\sigma_y^{\text{reg}},0)}{F_{0y}(0,\sigma_y^{\text{reg}},0)}\sin(\beta')$$

$$= \frac{t_{0a}(\sigma_x, \sigma_y, \gamma)}{F_{0y}(0, \sigma_y^{\text{reg}}, 0)} (F_{ay,slip}(\sigma_x, \sigma_y, \gamma) - F_{ay,slip}(0, \sigma_y^{\text{reg}}, 0) \sin(\beta'))$$
$$= \frac{a}{3} \frac{(4\psi - 1)(1 - \psi)^2}{\Upsilon} \left(\frac{\sigma_y}{\sigma_y^\circ \psi} - \sin(\beta') \right) = \frac{a}{3} \frac{(4\psi - 1)(1 - \psi)^2}{\Upsilon} \left(\frac{\sin(\beta)}{\sigma_y^\circ \Lambda} - \sin(\beta') \right) \tag{57}$$

where t_a is the pneumatic trail for the adhesive region defined as

$$t_a(\sigma_x, \sigma_y, \gamma) = \frac{M_{az}(\sigma_x, \sigma_y, \gamma)}{F_{ay,slip}(\sigma_x, \sigma_y, \gamma)} \tag{58}$$

Finally

$$G_{camz} = \frac{M_{z,cam}(\sigma_x, \sigma_y, \gamma)}{F_{cam}(0, \sigma_y^{\text{reg}}, 0)} \tag{59}$$

simply derived from Equation (25) and (15).

A.5 Use of slip expressed in λ and α

In many occasions the slip expressed in λ and α is more convenient to use. The pure-slip tire forces are also mostly expressed as functions of these slips. Here follows guidelines for necessary conversions if λ and α are preferred. Calculate $\psi(\sigma_x, \sigma_y, \gamma)$ and use the following formulas

$$\sigma_x = \frac{\lambda}{1 - \lambda}; \qquad \sigma_y = \frac{\tan(\alpha)}{1 - \lambda} \tag{60}$$

The

$$\sigma_x^\circ = \frac{\lambda^\circ}{1 - \lambda^\circ}; \qquad \sigma_y^\circ = \tan(\alpha^\circ) \tag{61}$$

For the adhesive force use the force given at the pure-slip

$$\lambda_{0a} = \lambda \tag{62}$$

$$\alpha_{0a} = \arctan\left(\frac{\tan(\alpha)}{1 - \lambda} \right) \tag{63}$$

$$\lambda_{0s} = \frac{v}{v_0} \sqrt{(\lambda \cos(\alpha))^2 + \sin^2(\alpha)} \operatorname{sgn}(\lambda) \tag{64a}$$

$$\sin(\alpha_{0s}) = \frac{v}{v_0} \sqrt{(\lambda \cos(\alpha))^2 + \sin^2(\alpha)} \operatorname{sgn}(\alpha) \tag{64b}$$

$$\sigma_{0x}^{\text{reg}} = \sigma_x^\circ \sqrt{\left(\frac{\lambda}{1 - \lambda} \frac{1}{\sigma_x^\circ} \right)^2 + \left(\frac{\tan(\alpha)}{1 - \lambda} \frac{1}{\sigma_y^\circ} \right)^2} \operatorname{sgn}(\lambda) \tag{65a}$$

$$\sigma_{0y}^{\text{reg}} = \sigma_y^\circ \sqrt{\left(\frac{\lambda}{1 - \lambda} \frac{1}{\sigma_x^\circ} \right)^2 + \left(\frac{\tan(\alpha)}{1 - \lambda} \frac{1}{\sigma_y^\circ} \right)^2} \operatorname{sgn}(\alpha) \tag{65b}$$

$$\tan(\beta) = \frac{\sin(\alpha)}{\lambda \cos(\alpha)} \tag{66}$$